Oral presentation | Fluid-structure interaction

Fluid-structure interaction-I

Mon. Jul 15, 2024 10:45 AM - 12:45 PM Room A

[1-A-02] Effects of airfoil shapes on double transonic dip behaviors in supercritical airfoil flutter

*Eishu Kawashiro[1], Toma Miyake[1], Hiroshi Terashima[1] （1. Hokkaido University）

Keywords: Wing Flutter, Supercritical Airfoils, Double Transonic Dip, Boundary Layer Separation, Shock Waves

Effects of airfoil shapes on double transonic dip behaviors in supercritical airfoil flutter

E. Kawashiro[*], T. Miyake[*] and H. Terashima[*]
Corresponding author: kawashiro.eishu.t1@elms.hokudai.ac.jp
* Hokkaido University, N13 W8, Kita-ku, Sapporo, Hokkaido, Japan

1   Introduction

During aircraft flight, a self-induced vibration phenomenon known as flutter may occur, especially in the transonic flow regime, which is commonly referred to as the transonic dip phenomenon [1]. Many experiments and numerical simulations have been conducted on conventional, symmetrical airfoils, and their flutter characteristics are well understood. On the other hand, there are fewer studies on the flutter characteristics of supercritical airfoils currently used in high-speed aircraft. In previous flutter experiments of supercritical airfoils, Persoon et al. [2] observed a notable occurrence of double transonic dip behaviors. This phenomenon involves two distinct transonic dips: a typical transonic dip (first dip) and a second transonic dip at higher Mach numbers. However, the underlying mechanisms behind the double transonic dip behaviors remained unclear. Miyake et al. [3] recently conducted numerical simulations that successfully captured double transonic dip behaviors in supercritical airfoil flutter. They demonstrated that the cycle of separation and reattachment over the lower surface near the trailing edge of the supercritical airfoil (highly cambered surface) significantly contributes to generating the second transonic dip. These findings highlight the substantial influence of airfoil shape on the occurrence of double transonic dip behaviors. Thus, this study aims to clarify the effects of airfoil shapes on double transonic dip behaviors in supercritical airfoil flutter.

2   Numerical computing methods

2.1   Fluid equation

The governing equations for the fluid were the two-dimensional unsteady Reynolds-averaged compressible Navier-Stokes (URANS) equations. The turbulent viscosity was estimated using the Spalart-Allmaras (SA) turbulence model [4]. SHUS [5] was used to evaluate the inviscid numerical flux, and MUSCL [6] with the van Albada limiter was employed to achieve high-order accuracy. For time integration, the LU-SGS [7] implicit algorithm was used.

2.2   Structural equation

Figure 1 depicts a two-dimensional airfoil structure model [8]. The structural model has two degrees of freedom (2-DOF): vertical displacement h (positive downward in the z direction) and rotational displacement α (positive head-up). The governing equations are nondimensionalized and written in matrix form as follows:

$$\begin{bmatrix} 1 & x_\alpha \\ x_\alpha & r_\alpha^2 \end{bmatrix} \begin{Bmatrix} \ddot{\bar{h}} \\ \ddot{\alpha} \end{Bmatrix} + \begin{bmatrix} (\omega_h / \omega_\alpha)^2 & 0 \\ 0 & r_\alpha^2 \end{bmatrix} \begin{Bmatrix} \bar{h} \\ \alpha \end{Bmatrix} = \{\boldsymbol{Q}\}$$

$$\{\boldsymbol{Q}\} = \frac{V_*^2}{\pi} \begin{Bmatrix} -C_l \\ 2C_m \end{Bmatrix}, \quad V_* = \frac{U_\infty}{b\omega_\alpha\sqrt{\mu}}, \quad \mu = \frac{m}{\rho_\infty b^2 \pi}$$

(1)

The vertical displacement h and time t are nondimensionalized using the half-wing chord length $b (= c / 2)$ and the angular frequency of rotational motion ω_α, respectively. m is the mass per unit length, C_l is the lift coefficient (positive in the z direction in the figure), and C_m is the moment around the elastic axis (positive head-up). ω_h and ω_α are uncoupled circular bending and pitching frequencies, respectively. U_∞ and ρ_∞ are the freestream flow velocity and density, respectively. V_* is the speed index, and μ is the mass ratio. Structural damping has not been

considered in this study. The time integration method for the structural equation was the fourth-order Runge-Kutta method.

The airfoils used in this study have asymmetrical surfaces, resulting in non-zero aerodynamic forces at an angle of attack of 0 degrees. To start the coupled calculations at arbitrary angles, a steady-state lift coefficient $C_{l,0}$ and a moment coefficient $C_{m,0}$ were added to the force vector $\{Q\}$ of equation (1). The modified force vector is expressed as follows:

$$\{Q\} = \frac{V_*^2}{\pi} \begin{Bmatrix} -(C_l - C_{l,0}) \\ 2(C_m - C_{m,0}) \end{Bmatrix}. \tag{2}$$

2.3   Coupled procedure

The coupled fluid-structure interaction was performed using a weekly coupling method, where the aerodynamic and structural dynamics equations were solved separately in the temporal direction.

  (a) The flow field around a static airfoil is obtained.
  (b) A small acceleration is imposed on the airfoil.
  (c) The Navier-Stokes equations are solved to calculate the aerodynamic forces C_l and C_m.
  (d) The obtained C_l and C_m are substituted into the structural equation (1) and a structural calculation is performed to determine new displacements h and α.
  (e) The airfoil grid is moved using the new displacements.
Steps (c)-(e) were repeated iteratively.

2.4   Computational conditions

The camber near the trailing edge of the SC2-0610 airfoil (baseline) was adjusted to investigate the impact of airfoil shapes on double transonic dip behaviors. Figure 2 depicts the profiles of each airfoil used in this study. A lower camber airfoil is labeled as the 0.0% camber airfoil (trailing edge at y/c = 0.0), while a higher camber airfoil is designated as the -3.0% camber airfoil (trailing edge at y/c = -0.03). The number of grid points was 1209×250 for all airfoils. The grid is regenerated at each time step in the flutter calculations based on the airfoil displacement and angle. The method of Melville et al. [9] was used for this analysis. In the structural equation (1), the structural parameters were $x_\alpha = 1.8$, $r_\alpha^2 = 3.48$, $a = -2.0$, $\mu = 60$, $\omega_h = \omega_\alpha = 100 \text{ rad/s}$. These parameters are commonly employed in transonic flutter simulations [8,10]. The freestream Mach number, Reynolds number, and angle of attack were set to $0.7 - 0.9$, 6.6×10^6, and 0 deg, respectively.
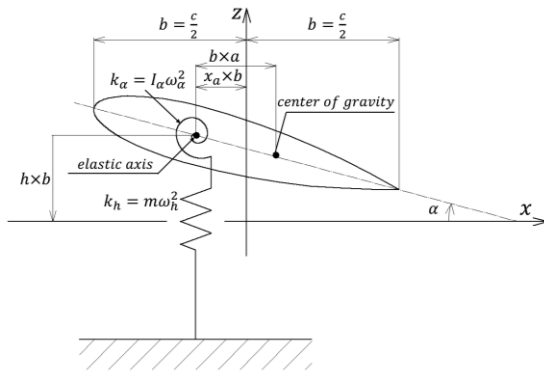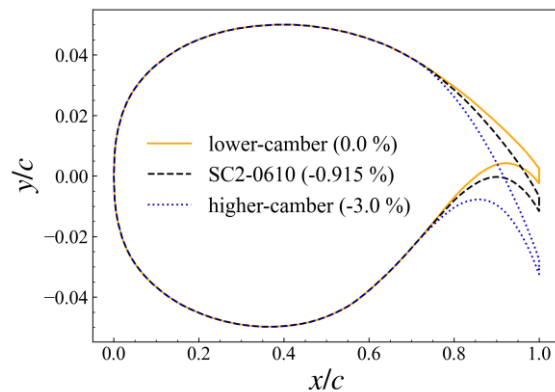

Fig. 1 2-DOF wing section model

Fig. 2 SC2-0610 (baseline) and modified airfoil shapes

2

3 Results and discussions

Figure 3 compares the flutter speed and frequency obtained with three different airfoils. The flutter velocity V_*, where the airfoil vibration amplitude remains constant, was defined as the flutter boundary, and the vibration frequency at that point was identified as the flutter frequency. The flutter speed of the SC2-0610 airfoil (black line) significantly decreases at $M_\infty = 0.775$ and 0.855, exhibiting the double transonic dip observed in experiments. Similarly, the airfoil with -3.0% higher camber (blue line) exhibits a decrease in flutter speed at $M_\infty = 0.725$ and 0.885, while the airfoil with 0.0% lower camber (orange line) shows double dips at $M_\infty = 0.800$ and 0.855. The trend suggests they also experience double transonic dip phenomena similar to the SC2-0610 airfoil. However, the Mach number where these dips occur varies depending on the airfoil shape. For the airfoil with -3.0% higher camber, the first dip shifts to the low Mach number side, and the second dip shifts to the high Mach number side. In contrast, for the airfoil with 0.0% lower camber, the first dip moves toward the high Mach number side, and the second dip moves toward the low Mach number side. The results of flutter frequency indicate that the first-order bending mode is dominant in both the first-dip and second-dip regions for all airfoils. At high Mach numbers, the airfoil with -3.0% higher camber exhibits multiple flutter boundaries even at a Mach number condition, and the airfoil oscillates in the second-order torsional mode.

The flutter characteristics of the SC2-0610 airfoil discussed in previous research [3] are briefly summarized here. Similar to conventional symmetrical airfoils, the first dip is caused by a delay in the phase of the shock wave motion over the upper surface, resulting in a phase delay of the aerodynamic force against the airfoil motion. Subsequently, the system recovers from the first dip because of a phase advance feature of the aerodynamic force caused by separation behind the shock wave [11]. The second dip occurs when the flow behind the shock wave over the lower surface is repeatedly separated and reattached during oscillations, leading to a phase advance of the shock wave motion over the upper surface [3]. Consequently, this phase advance feature of the shock wave motion turns to a phase delay of the aerodynamic force against airfoil motion, causing the system to be unstable. As the Mach number increases, the flutter speed increases again because the flow behind the shock waves over the upper and lower surfaces becomes fully separated during oscillation.
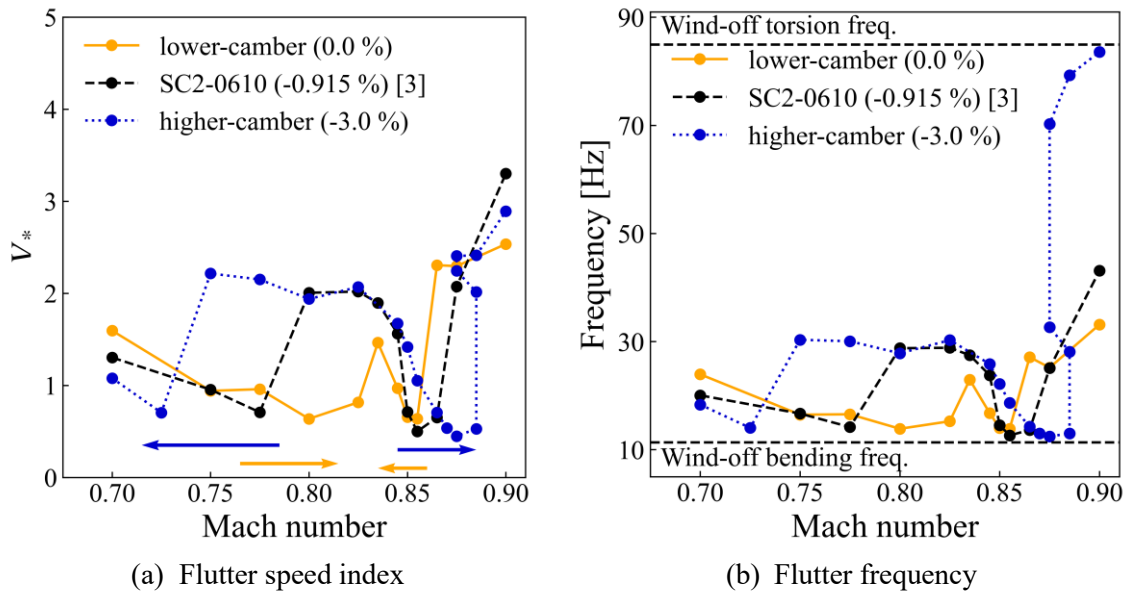

(a) Flutter speed index   (b) Flutter frequency

Fig. 3 Flutter boundaries

3.1   Effects of airfoil shape on first dip

Figures 4 and 5 show the flow field around the baseline (SC2-0610) and modified (0.0% and -3.0% camber) airfoils at two Mach numbers ($M_\infty = 0.775$ and 0.800). In Fig. 4 ($M_\infty = 0.775$), the 0.0% airfoil exhibits no shock wave and boundary layer separation. On the other hand, a shock wave forms over the upper surface for the SC2-0610 and -3.0% camber airfoils. Furthermore, a separation region develops over the upper surface of the -3.0% camber airfoil. Thus, the -3.0% camber airfoil recovers from the first dip at $M_\infty = 0.775$ due to a phase advance feature of shock wave motion with separation [8], causing the first dip to shift towards the lower Mach number side. On the other hand, at $M_\infty = 0.800$, boundary layer separation behind the shock wave is observed over the upper surface of the SC2-0610, enabling it to recover from the first dip at that Mach number condition. For the 0.0% camber airfoil, boundary layer separation behind the shock wave occurs at higher Mach numbers, leading to the first dip occurring at the higher Mach numbers. In summary, as the airfoil camber near the trailing edge increases, the occurrence of the first dip shifts towards the lower Mach number side. Conversely, lower camber airfoils tend to exhibit the first dip at higher Mach numbers.
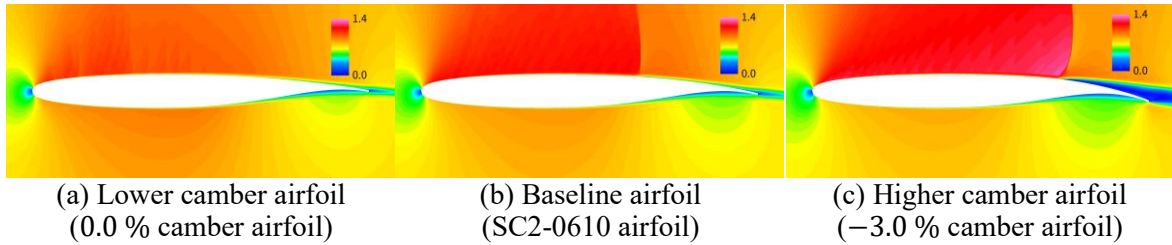

(a) Lower camber airfoil
(0.0 % camber airfoil)

(b) Baseline airfoil
(SC2-0610 airfoil)

(c) Higher camber airfoil
(−3.0 % camber airfoil)

Fig. 4 Comparisons of Mach number distributions at $M_\infty = 0.775$

(a) Lower camber airfoil
(0.0 % camber airfoil)

(b) Baseline airfoil
(SC2-0610 airfoil)
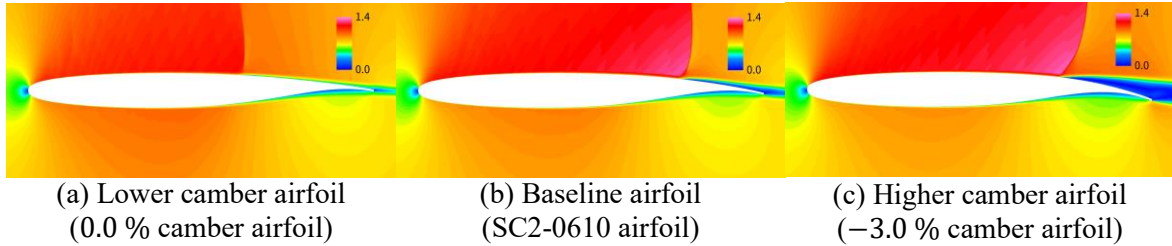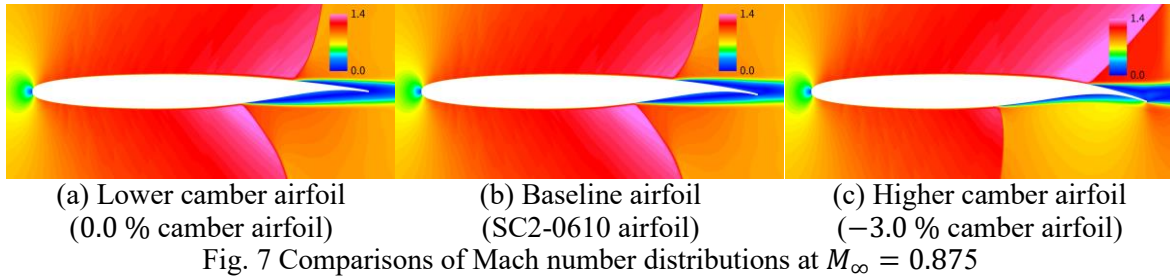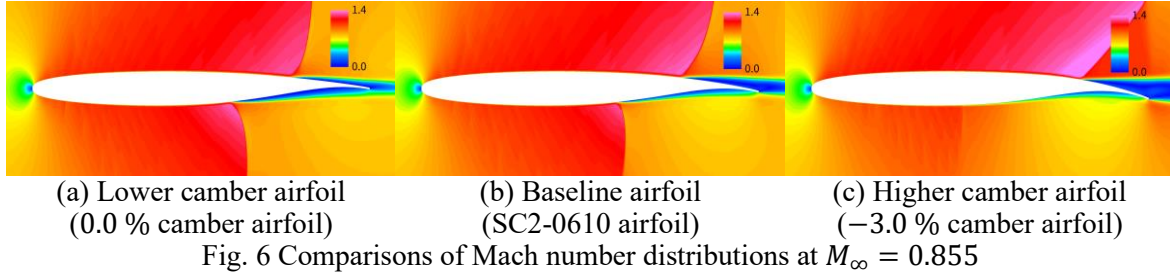
(c) Higher camber airfoil
(−3.0 % camber airfoil)

Fig. 5 Comparisons of Mach number distributions at $M_\infty = 0.800$

3.2   Effects of airfoil shape on second dip

Fig. 6 depicts boundary layer separation occurring near the trailing edge over the lower surface of the 0.0% camber and SC2-0610 airfoils at $M_\infty = 0.855$. Although now shown here, the flow behind the shock wave over the lower surface exhibits repeated separation and reattachment during oscillations. As demonstrated in the previous study [3], this cycle induces negative damping on the airfoil motion by influencing the shock wave dynamics over the upper surface. Thus, a second dip is observed at $M_\infty = 0.855$ with these airfoils. On the other hand, the -3.0% camber airfoil shows no separation with a weak shock wave over the lower surface, resulting in the absence of the second dip at this Mach number condition. At an increased Mach number ($M_\infty = 0.875$), as shown in Fig. 7, the separation region over the lower surface of the 0.0% camber and SC2-0610 airfoils expands, and the boundary layer behind the shock wave is fully separated during oscillations. Consequently, these two airfoils recover from the second dip. In contrast, the boundary layer of the -3.0% camber airfoil undergoes repeated separation and reattachment during oscillations, leading to instability and resulting in the occurrence of the second dip at this Mach number condition. In summary, concerning the second dip, as the airfoil camber near the trailing edge increases, the Mach number condition at which the flow undergoes repeated separation and reattachment over the lower surface also increases. Consequently, the occurrence of the second dip shifts to higher Mach numbers.

4

(a) Lower camber airfoil
(0.0 % camber airfoil)

(b) Baseline airfoil
(SC2-0610 airfoil)

(c) Higher camber airfoil
(-3.0 % camber airfoil)

Fig. 6 Comparisons of Mach number distributions at $M_{\infty} = 0.855$

(a) Lower camber airfoil
(0.0 % camber airfoil)

(b) Baseline airfoil
(SC2-0610 airfoil)

(c) Higher camber airfoil
(-3.0 % camber airfoil)

Fig. 7 Comparisons of Mach number distributions at $M_{\infty} = 0.875$

4   Conclusion

This study numerically investigated the effect of supercritical airfoil shape on transonic dip phenomena. In addition to the SC2-0610 airfoil, two modified airfoils derived from the original SC2-0610 airfoil were used for investigation: one with higher camber and another with lower camber. The following conclusions were drawn.

(a) All airfoils exhibited double transonic dip behaviors in their flutter boundary curve despite variations in trailing edge camber.

(b) The first dip: Increasing camber shifted the location of the first dip towards lower Mach numbers. This shift was attributed to the higher camber, which caused shock wave generation over the upper surface at lower Mach numbers.

(c) The second dip: Increasing camber moved the location of the second dip towards higher Mach numbers. This shift occurred because higher camber delayed the occurrence of the repeated separation and reattachment cycle of the boundary layer over the lower surface at higher Mach numbers.

This study highlighted the significant influence of the trailing edge camber on the Mach number conditions governing the occurrence of double transonic dip phenomena in supercritical airfoil flutter.

References

[1]   W. J. Mykytow. A Brief Overview of Transonic Flutter Problems. Unsteady Airloads in Separated and Transonic Flow, AGARD-CP-226, 11-1-11-11, 1977.

[2]   A. J. Persoon, J. J. Horsten and J. J Meijer. Measurement of Transonic Dips in the Flutter Boundaries of a Supercritical Wing in a Wind Tunnel. Journal of Aircraft, 21: 906-912, 1984.

[3]   T. Miyake and H. Terashima. Numerical Investigation of Double Transonic Dip Behaviors in Supercritical Airfoil Flutter. AIAA Journal, 61: 5365-5376, 2023.

[4]   P. R. Spalart and S. R. Allmaras. A One-Equation Turbulence Model for Aerodynamic Flows. AIAA Paper 1992-0439, 1992.

[5]   E. Shima, and T. Jounouchi. Role of CFD in Aeronautical Engineering (No. 14). AUSM Type Upwind Schemes. NAL SP-34, Japan, 1997.

[6]   W. K. Anderson, J. L. Thomas, and B. V. Leer. Comparison of Finite Volume Flux Vector Splittings for the Euler Equations. AIAA Journal, 24: 1453-1460, 1986.

[7]   S. Yoon, and A. Jameson. Lower-Upper Symmetric-Gauss-Seidel Method for the Euler and Navier-Stokes Equations. AIAA Journal, 26: 1025-1026, 1988.

[8]   K. Isogai. On the Transonic-Dip Mechanism of Flutter of a sweptback wing. AIAA Journal, 17: 793-795, 1979.

[9]   R. B. Melville, S. A. Morton, and D. P. Rizzetta. Implementation of a Fully-Implicit, Aeroelastic Navier-Stokes Solver. AIAA Paper 1997-2039, 1997.

[10] K. Isogai. Transonic-Dip Mechanism of Flutter of a sweptback wing: Part II. AIAA Journal, 19: 1240-1242, 1981.

[11] N. D. Oyeniran, T. Miyake, H. Terashima, R. Seki, K. Ishiko and T. Nonomura. Unsteady Aerodynamics Around a Pitching Airfoil with Shock and Shock-Induced Boundary-Layer Separation. AIAA Journal, 60: 6557-6565, 2022.